Solubility of Nanocrystalline Cerium Dioxide: Experimental Data and Thermodynamic Modeling

Tatiana V. Plakhova[1)], Anna Yu. Romanchuk[1)], Sergey N. Yakunin[2)], Thomas Dumas[3)], Selvan Demir[4),5)], Shuao Wang[4),5)], Stefan G. Minasian[5)], David K. Shuh[5)], Tolek Tyliszczak[6)], Andrey A. Shiryaev[1),7)], Alexander V. Egorov[1)], Vladimir K. Ivanov[1),8),9)], Stepan N. Kalmykov[,1),2)]*

1) Lomonosov Moscow State University, Moscow, Russia

2) National Research Centre "Kurchatov Institute", Moscow, Russia

3) CEA/DEN/MAR/DRCP, Nuclear Energy Division, Radiochemistry and Process Department, BP17171, 30207 Bagnols sur Cèze, France

4) Chemical Sciences Division, Lawrence Berkeley National Laboratory, Berkeley, CA 94720, USA

5) Department of Chemistry, University of California, Berkeley, CA 94720, USA

6) Advanced Light Source, Lawrence Berkeley National Laboratory, Berkeley, California 94720, USA

7) Frumkin Institute of Physical Chemistry and Electrochemistry of Russian Academy of Science, Moscow, Russia

8) Kurnakov Institute of General and Inorganic Chemistry, Russian Academy of Sciences, Moscow, Russia

9) National Research Tomsk State University

*corresponding author: stepan@radio.chem.msu.ru, phone number: +7-495-939-3220

ABSTRACT

Ultrafine 5 nm ceria isotropic nanoparticles were prepared using the rapid chemical precipitation approach from cerium(III) nitrate and ammonium hydroxide aqueous solutions. The as-prepared nanoparticles were shown to contain predominantly Ce(IV) species. The solubility of nanocrystalline CeO_2 at several pH values was determined using ICP-MS and radioactive tracer methods. Phase composition of the ceria samples remained unchanged upon partial dissolution, while the shape of the particles changed dramatically, yielding nanorods under neutral pH conditions. According to X-ray absorption spectroscopy investigation of the supernatant, Ce(III) was the main cerium species in solution at pH < 4. Based on the results obtained, a reductive dissolution model was used for data interpretation. According to this model, the solubility product for ceria nanoparticles was determined to be $\log K_{sp}$ = -59.3 ± 0.3 in 0.01M $NaClO_4$. Taken together, our results show that the pH-dependence of ceria anti- and pro-oxidant activity can be related to the dissolution of CeO_2 in aqueous media.

INTRODUCTION

Nanosized cerium oxide (nano-ceria) is currently one of the most widely used engineered nanomaterials [1-13]. Ceria nanoparticles (NPs) exhibit high oxygen storage capacity, good chemical and thermal stability and excellent biocompatibility. Nano-ceria has already been widely used as a component of various catalysts, protective corrosion-resistant coatings for metals and alloys, polishing mixtures and abrasives [1-3, 12, 13]. It is anticipated that the production of engineered ceria-based nanomaterials will notably increase in the immediate future, because of emerging ceria

applications in UV filters [4, 5, 14], solid oxide fuel cells [6, 7, 14-18] and pharmacology [8-11]. Rapidly growing demand in ceria-based materials inevitably results in their release to the environment (e.g. with industrial wastewaters) that could affect the biota [19-22].

The biological effect of the cerium compounds depends on its valence state. Toxicity of Ce(IV) compounds is associated primarily with high redox potential of tetravalent cerium ions and their ability to oxidize biomolecules. The standard electrode potential of Ce^{4+}/Ce^{3+} (+1.72V) is much higher than the oxidation potential of the most organic compounds (for example, for growth nutrient Dulbecco's Modified Eagle's Medium, this value lies in the range of -0.38 to +0.34 V [23]). It was also found [24] that the biological activity of Ce(III) compounds is probably dictated by proximity of the ionic radii of Ce^{3+} and Ca^{2+} ions (1.01 Å and 1.00 Å, respectively) [25]. As a result, calcium ions in biomolecules can be partially replaced by cerium ions. Additionally, reducibility of ceria determines its activity in biochemical redox processes (especially inactivation of reactive oxygen species (ROS) and free radicals in living cells), and underlies its application as an antioxidant / prooxidant [26-33].

The redox activity of ceria is often associated with the hypothesis of its high oxygen non-stoichiometry. However, this hypothesis is still debatable. Analyzing a range of studies of cerium oxidation state performed by X-ray photoelectron spectroscopy (XPS) [34-36], X-ray absorption spectroscopy (XAS) [35, 37, 38], electron energy loss spectroscopy (EELS) [39, 40] and UV-visible spectroscopy [41], one can conclude that oxidation state measurements strongly depend on the technique used. Tsunekawa et al. [42-44] estimated the dependency of the ceria lattice parameters on the particles' size. Their calculations showed that, at a ceria particle size of 1.9 nm, the full conversion of $Ce^{4+} \rightarrow Ce^{3+}$ should occur. The XPS results of Deshpande et al. [34] also showed an increasing of cerium(III) concentration in CeO_2 with a decrease in particle size. The EELS data of Goris et al. [39] suggested that distribution of Ce^{3+} in CeO_2 particles is uneven. A thick layer of Ce^{3+} is present on the <001> surface while Ce^{4+} concentrates on the <111> facet. In turn, Paun et al. [37]

found that there was no significant Ce(III), even in small ceria nanoparticles, according to the Ce L_3 XAS technique.

It is generally believed that cerium dioxide has extremely low solubility, which has little or no effect on its cytotoxicity [45]. A number of recent studies have shown that ceria undergoes partial dissolution under specific conditions [40, 46, 47]. Nevertheless, there are still no reliable experimental solubility data for CeO_2 in bulk and nanoparticles. Existing estimates ($\log Ksp = -60$) for cerium dioxide are based on theoretical calculations [45]. Dahle et al. [40] attempted to measure experimentally the release of Ce from commercially available CeO_2 NPs using ICP-AES at various pH values. The release of Ce was found to be three times greater for large NPs than for small NPs. Such behaviour is quite unusual, since the reactivity of nanoparticles generally increases with a decrease in particle size [48]. Unfortunately, Dahle et al. [40] did not vary particle size in a systematic way while keeping the amount of material constant.

An accurate study of ceria solubility is in great demand, to find out the possible interaction mechanisms of CeO_2 nanoparticles with living beings, and to obtain deeper insights into the negative or positive effects that can be caused by ceria dissolution in biological media. The latter is extremely important in light of possible biomedical applications of nano-ceria. Obtaining the solubility product constant allows modeling of CeO_2 behaviour *in vivo* by taking into account complexation reactions of cerium species, with various anions such as carbonate, chloride, phosphate and others, and by considering other pe+pH conditions. Therefore, the purpose of this paper is to experimentally determine the solubility of cerium dioxide nanoparticles in a broad pH range, and to develop a thermodynamic model describing the dissolution process. It is a known fact that many factors can affect the solubility behaviour of nanoparticles. These factors are generally of two types: solution composition and properties (pH value, ionic strength, the presence of carbonates, etc.), and solid state characteristics (particle size, morphology, synthesis routs, aggregation degree,

etc.). Therefore, in this paper, for a better understanding of the solubility behaviour of CeO_2 nanoparticles, and to enable thermodynamic modeling, both solid and aqueous phases were examined simultaneously.

EXPERIMENTAL SECTION

Synthesis of CeO_2 nanoparticles

In the present study, ceria nanoparticles were prepared according to the previously established protocol [49]; 50 ml of 0.1 M cerium(III) nitrate aqueous solution was added to 250 ml of aqueous ammonia (3M), at room temperature, under continuous stirring. The precipitate formed was allowed to age for 12 hours. After precipitation, all the samples were washed three times with Milli-Q water (18.4 MOhm/cm).

In some experiments, an aliquot of a mixture of radioactive tracers ^{141}Ce ($T_{1/2}$ = 32.5 days) and ^{144}Ce ($T_{1/2}$ = 284.9 days) was added to initial Ce(III) nitrate stock solution. The mixture of these γ-emitting isotopes was isolated from a thorium target irradiated by medium-energy protons, as described previously [50]. Radioactive cerium isotopes were added as cerium(III) nitrate; the chemical form is the same as for the stable cerium. The ratio of stable and radioactive isotopes was fixed in these experiments and varied in the range of 1×10^7 imp/s per mole of stable Ce to 1×10^9 imp/s per mole of stable Ce, depending on experimental conditions.

Characterization of CeO_2 nanoparticles

Ceria nanoparticles were analyzed before and after solubility studies, to determine phase composition, morphology of the particles and the valence state of cerium.

The X-ray diffraction (XRD) data were recorded using a Bruker D8 Advance diffractometer, (CuKα radiation). The PC-PDF database was used for the identification of the crystalline phases. Particle size of nanocrystalline ceria was calculated using the Scherrer formula, where the coefficient of anisotropy (*K*-factor) was set to 1. Line profiles for (111) and (200) reflections were

fitted to pseudo-Voigt functions. Particle size was calculated from full width at half maximum (FWHM) of (111) and (200) diffraction lines. No traces of amorphous phases in the XRD pattern were detected.

Microstructural evaluation studies were performed using a Libra 200 Carl Zeiss, and a Jeol-2100F, transmission electron microscopes (HRTEMs) with accelerating voltages of 200 kV. Electron diffraction patterns were recorded using the same instruments.

Small-angle X-ray scattering patterns were registered using monochromatic CuKα-radiation in a broad angular range, (scattering vectors(s) between 0.1–27 nm^{-1}), using a SAXSess diffractometer (Anton Paar). Samples were placed in standard X-ray capillaries. A Kratki collimation scheme was used. Slit-geometry providing a highly intense primary X-ray beam was employed; reduction to point geometry (desmearing) was performed using a standard algorithm [51]. All measurements were performed at room temperature, in an evacuated chamber (residual pressure 5–10 mbar).

Soft X-ray spectromicroscopy was used for the investigation of the electronic structure and chemical composition of the CeO_2 nanoparticles. Single-energy images and O K-edge and Ce $M_{5,4}$-edge XANES spectra were acquired using the STXM instrument at the Environmental Science (MES) beamline 11.0.2 at the Advanced Light Source (ALS), which is operated in topoff mode at 500 mA, in a ~0.5 atm He-filled chamber [52-54]. These conditions allow for the study of air-dried samples, and this is significant, since cerium dioxide nanoparticles undergo partial reduction upon thermal treatment and exposure to reduced pressures. For the STXM measurements, an air-dried suspension of NPs was sandwiched between two Si_3N_4 windows, with data collected and processed as previously described [55, 56]. The maximum energy resolution $E/\Delta E$ was previously determined at better than 7500. For these measurements, the X-ray beam was focused with a zone plate onto the sample, and the transmitted light was detected. The spot size and spectral resolution were determined from characteristics of the 25 nm zone plate. Images at a single energy were obtained by

raster-scanning the sample and collecting transmitted monochromatic light as a function of sample position. Elemental maps were obtained by subtraction one image taken at an energy just below the edge from another taken at the absorption maximum, such that lighter regions correspond to greater concentration of the absorbing atom. Spectra at particular regions of interest on the sample image were extracted from the "stack", which is a collection of images recorded at multiple, closely spaced photon energies across the absorption edge. To quantify the absorbance signal, the measured transmitted intensity (I) was converted to optical density using Beer−Lambert's law: $OD = \ln(I/I_0) = \mu\rho d$, where I_0 is the incident photon flux intensity, d is the sample thickness, and μ and ρ are the mass absorption coefficient and density of the sample material, respectively. Incident beam intensity was measured through the sample-free region of the Si_3N_4 windows. Regions of particles with an absorption of >1.5 OD were omitted to ensure the spectra were in the linear regime of the Beer−Lambert law.

X-ray photoelectron spectroscopy (XPS) of the ceria samples was performed using a Kratos Axis Ultra DLD spectrometer (X-ray source - monochromatized Al Kα and calibration at the C1s (284.8 eV)). Pass energy was 160 eV for the wide-scan registration and 40 eV for the cerium 3d XPS line registration.

Solubility study

The solubility experiments were conducted batchwise, in 50 ml plastic vials. The pH of all suspensions was set in the range 1-11 by the sequential adding of small amounts of NaOH and $HClO_4$ solutions of known concentrations. Ionic strength was kept constant at 0.01M by adding an appropriate amount of $NaClO_4$ stock solution. The experiments with pH≥5 were conducted in a glove box under N_2 atmosphere, to prevent the formation of carbonate complexes.

Cerium concentration in the supernatant solutions was detected after centrifugation at 40,000 g for 4 hours (Allegra 64R, Beckman Coulter). Cerium concentration in the solutions prepared at pH≤5

was determined by the Inductively Coupled Plasma Mass Spectrometry (ICP-MS) method (Agilent 7500). At pH>5, where the solubility of CeO_2 was found to be very low, cerium concentration in the solutions in this case was analyzed by γ-spectroscopy (GC-3020, Canberra Packard Ind.). The total concentration of cerium in solution was then recalculated using the ratio of stable and radioactive isotopes in initial isotopically-labeled CeO_2. A radioactive tracer technique was used to measure low cerium concentrations in solution, since the limit of detection is as low as 10^{-15} M.

The examination of the supernatants was performed one month after equilibration with the solids, since the kinetics data obtained at different pH values (Figure S_1 a, b) demonstrated that the steady state conditions were reached in 15 days (or less). To additionally confirm this, cerium concentration in the samples prepared at pH 2-6 was also measured after two, six and sixteen months. All the results were in good agreement, within the limits of experimental error (Figure S_1c).

Redox potentials E(mV) were measured with a Pt-electrode relative to a Ag/AgCl reference electrode, and were converted to Eh (Eh(mV) = E(mV) + 208 mV). The redox potential is usually given relative to the standard hydrogen electrode (SHE), or, analogous to pH, in terms of apparent electron activity ($pe = -\log a_{e^-}$). Eh and pe are related by $Eh = -(RT/F)\ln a_{e^-}$ where R is the universal gas constant, T is the temperature (K) and F is the Faraday constant (pe = 16.9 Eh (V) at 25°C). ZoBell's standard solution was used for the control. The Eh was directly measured in the suspensions during constant stirring. In each case, the measurements were performed until Eh value drift was less than 5 mV within 30 min.

X-ray absorption fine structure (XAFS)

In this study, we used the total-reflection XAFS (TR-XAFS) technique at the air-water interface, for the study of cerium oxidation state in supernatant solutions obtained through solubility experiments. The experiment was performed at the "Langmuir" beamline of Siberia II synchrotron radiation source (NRC "Kurchatov Institute"). The X-ray beam generated from a bending magnet in

the storage ring was monochromated using a Si(111) double crystal monochromator, and shaped using a slit with vertical and horizontal sizes of 0.1 and 5 mm, respectively. In contrast to a condensed-matter sample, most liquid surfaces cannot be positioned in the X-ray beam by being tilted into the conventional θ-2θ-geometry. Therefore, an additional, downwards-reflecting, optical scheme containing two total reflection mirrors was installed at the Langmuir beamline, enabling the tilting of the synchrotron radiation beam to the horizontally oriented liquid interface. The tilting module works such that, primarily, the X-ray beam is reflected upwards with the first quartz mirror, and then tilted downwards with the second, tungsten-coated, mirror. In this scheme, the angle of incidence of the X-rays to an interface can be changed whilst keeping the position of the beam fixed. The critical angle for a water surface near the Ce L_3-edge is 0.215°, and this angle only changes slightly over the range of a XANES energy scan. The angle of incidence was maintained close to, but below, the critical angle of total reflection, which provided the penetration depth of evanescent waves to 65 nm. Cerium solutions were placed in a 5x5 cm Teflon cell. The total sample volume was around 8 mL, taking into account the liquid surface meniscus. The XANES data were collected using the Ce-fluorescence signal that was extracted from the energy spectrum recorded using an energy dispersive Vortex EX detector positioned perpendicular to the surface.

RESULTS AND DISCUSSION

Ceria nanoparticles characterization

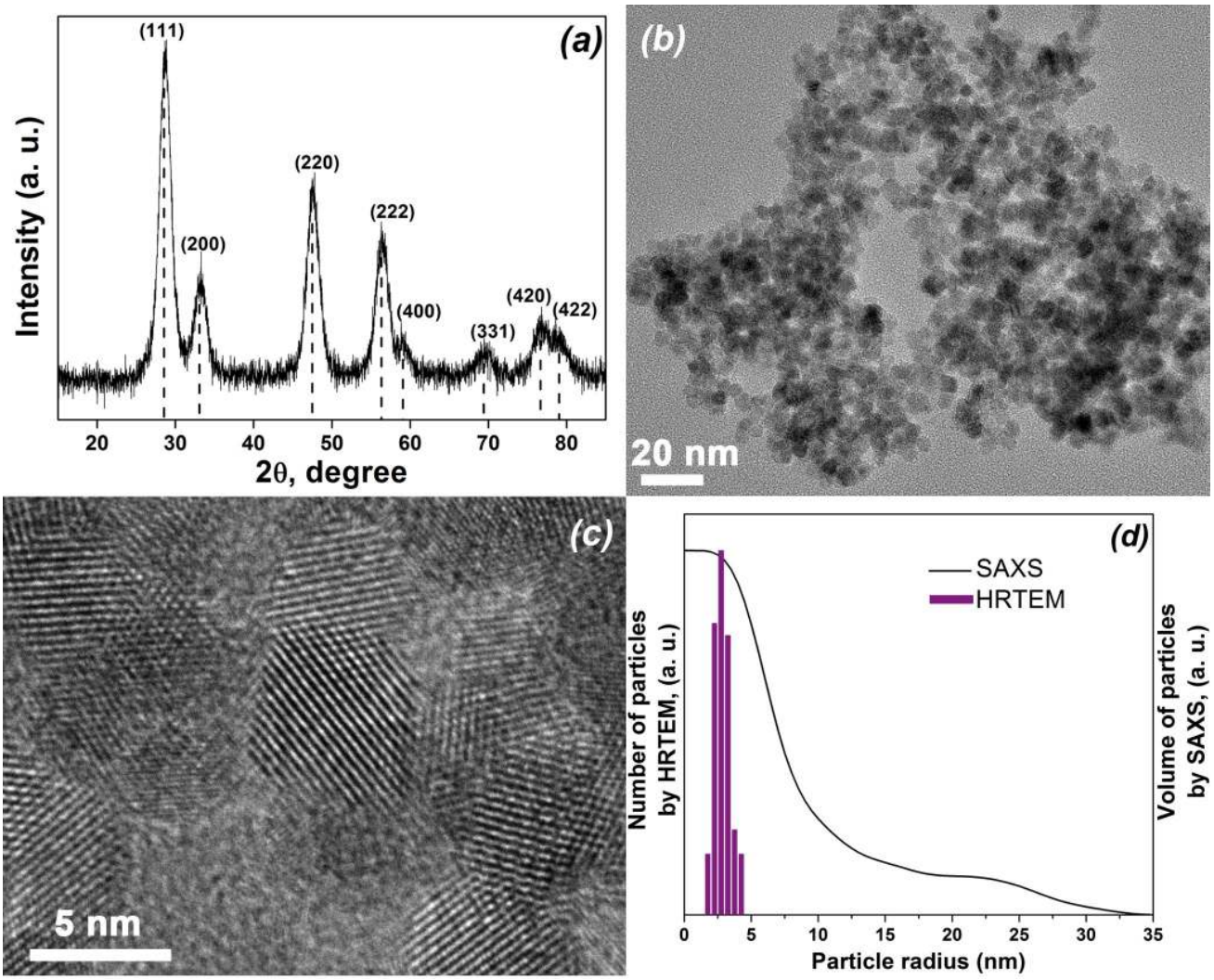

Figure 1. Characterization of as-prepared CeO_2 nanoparticles: a) XRD data; b), c) HRTEM data; d) CeO_2 NPs size distribution according to HRTEM and SAXS data.

According to XRD and selected area electron diffraction data, ultrafine CeO_2 nanoparticles with fluorite crystal structure (PCPDF [81-792]) were formed under chosen experimental conditions (Fig.1a). The average crystallite size of the as-prepared sample was 5.5 nm, as determined from XRD. The unit cell parameter for ceria sample was determined to be 5.421(2) Å, using the Rietveld refinement analysis of XRD pattern. The calculated unit cell parameter closely agreed with our previously reported data [49] and confirmed earlier suggestions that the ceria unit cell parameter increases with decreasing particle size [42, 43, 57-59]. Typical HRTEM images and particle size

distribution of the nanoparticles are shown in Figure 1(b,c,d). The particles obtained have a truncated octahedral habitus, that is in agreement with previously published data on computer simulation[60-62]. The mean diameter of cerium dioxide nanoparticles, as determined by measuring 200 nanoparticles, was 5.7±0.5 nm. As can be seen, the size of the crystallites determined from the XRD data coincided with the average size found from HRTEM data. The average particle size determination was also carried out using SAXS analysis. The data obtained by SAXS was a good reference point for both HRTEM and XRD analysis. Compared with HRTEM, it gave better statistics, and, in contrast to XRD, it did not require the drying of the samples (which might affect the results obtained [63]. Particle size distribution obtained from SAXS curve, using the GNOM program [64], is presented in Figure 1d; (corresponding experimental and theoretical scattering curves are shown in Figure S_2). Nanoparticles of 5 nm average size, as well as relatively large agglomerates up to 60 nm, were observed in the sample.

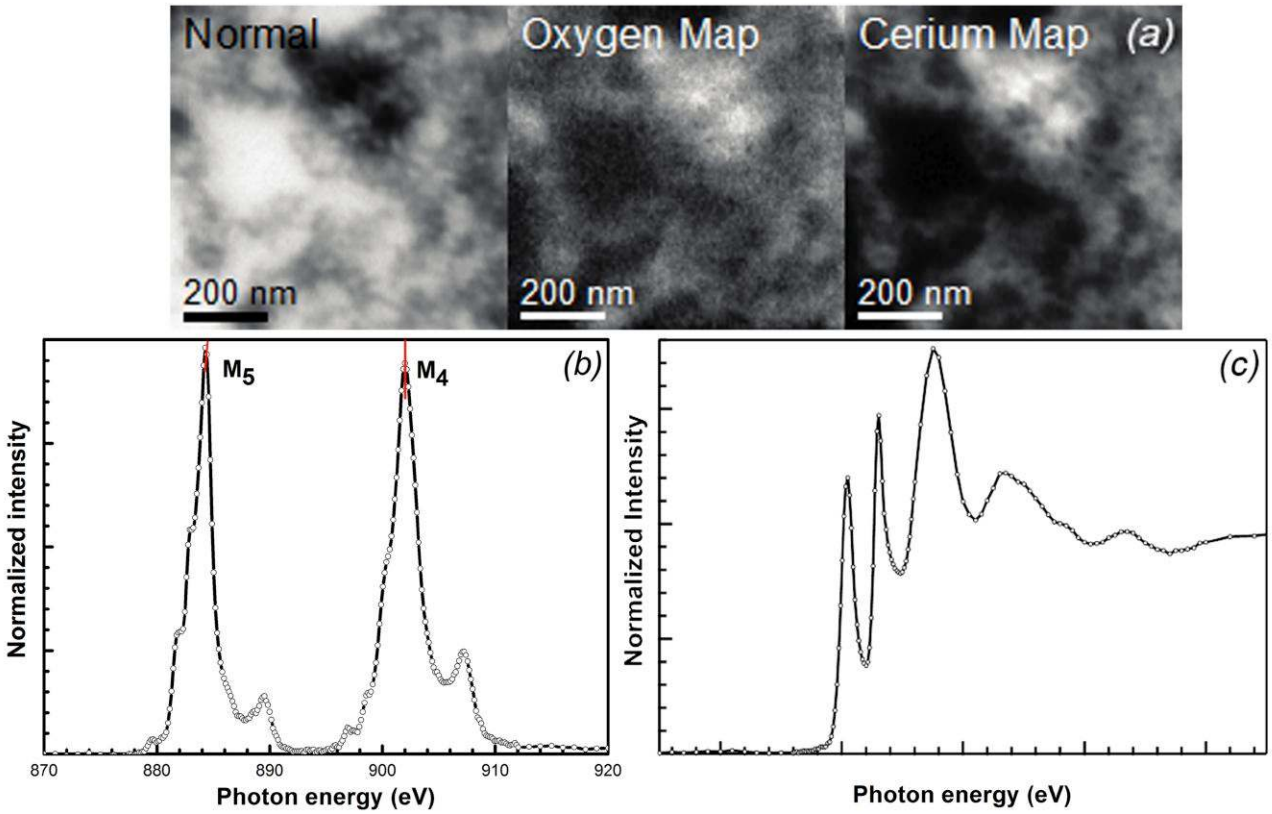

Figure 2. Images and spectra obtained using STXM-XAS for 50 nm diameter nanocrystalline CeO_2 agglomerates: a) normal contrast image and oxygen and cerium elemental maps; b) Ce $M_{4,5}$-edge XANES spectrum; c) oxygen K-edge spectrum.

X-ray absorption spectroscopy and scanning transmission X-ray microscopy (STXM-XAS) were used to evaluate bulk physical structure and chemical bonding. X-ray based microscopies such as STXM are ideal for sensitive inorganic materials such as CeO_2, because the measurements are conducted in an atmosphere of helium, and compositional changes that occur on exposure to vacuum or to an electron beam are more easily controlled. For these measurements, the spatial resolution was limited to 25 nm by the focusing ability of the X-ray optic, and the spectral resolution was better than 0.1 eV. Figure 2a shows the normal contrast images and elemental maps from freshly prepared (non-dried) ceria nanoparticles, the $CeM_{4,5}$-edge XANES spectrum collected in transmission (excitations from 3*d* to 4*f* electron core levels) (Figure 2b), and the oxygen K-edge spectrum from the same region. The Ce spectrum in Figure 2b was collected from a 50 nm diameter

cerium-rich region located from the Ce elemental map. Two characteristic peaks, with maxima at M_5=885 eV and M_4=904 eV, are present in the spectrum resulting from the spin orbit coupling of the 3d hole, along with associated fine structure. Previous works have shown that Ce-$M_{4,5}$-edge XANES spectra provide distinct signatures for the Ce^{3+} and Ce^{4+} oxidation states, although the ability to fully deconvolve mixtures of oxidation states is limited to about 5% for bulk materials [56, 65-67]. Spectra for the CeO_2 NPs closely resemble published O K-edge [68-70] and Ce $M_{5,4}$-edge[56, 66-68,71-73] spectra for CeO_2 obtained using a variety of detection methods, which confirms that subsequent solution-phase studies were conducted on analytes that were pure and homogenous. Some very small shape distortions of the spectrum can be attributed to either the presence of the surface hydroxyl groups, or Ce(III) at the NP interface. The present data agree well with previous works [37,41] in which the Ce(III)/Ce(IV) ratio in the samples prepared by similar chemical methods was determined by direct chemical methods and by measuring Ce-L_3-edge XANES, respectively. The oxygen K-edge in Fig. 2c also closely resembles that of CeO_2 [67].

To complement information from XANES studies, XPS was also used for the characterization of ceria samples. In contrast to the Ce-$M_{4,5}$-edge XAS investigation, the XPS study showed the presence of about 17% Ce(III) in the ceria sample. This discrepancy in the data can be explained by the partial reduction of Ce(IV) to Ce(III) under vacuum conditions. This assumption has been expressed previously [35, 74, 75]. In addition, these observations were substantiated experimentally by measuring the XPS spectra of CeO_2 samples immediately after placing them in the vacuum chamber, and after 12 hours' storage under vacuum conditions (Fig.S_3).

CeO_2 solubility measurements

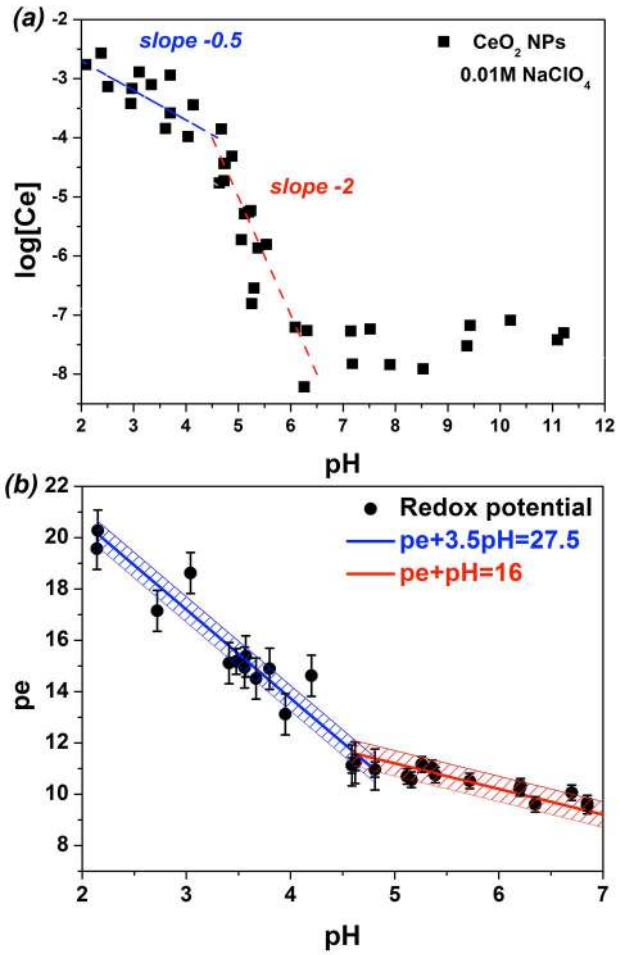

Figure 3. a) Solubility curve for 5 nm ceria NPs obtained using a combination of γ-spectroscopy and ICP-MS (I = 0.01 M $NaClO_4$); data in the acidic region were fitted using linear equations characterized by slopes of -0.5 and -2, respectively; b) experimental redox potential data collected from pH 2 to pH 7.

Figure 3a depicts experimental solubility data for ceria nanoparticles. The radioactive tracer approach was used for measuring CeO_2 solubility at pH > 5. Generally, with this method, a radioisotope is used to replace one or more atoms in the substance of interest; then, by detecting its radioactive decay, the concentration of both inactive and labelled atoms or ions can be measured. This method is commonly used for the determination of solubility of low-soluble compounds [76-79],

as it is more sensitive in comparison to ICP-MS. For cerium compounds, this method was used by Gelsema et al.[77] for a cerium (III) oxalate solubility study.

Data obtained indicate that ceria solubility in acidic solutions depends on the H^+ concentration, while in neutral and alkaline solutions ceria solubility is mostly pH independent. In turn, solubility data collected in the acidic pH region ($2 \leq pH \leq 7$) separated into two regions: $2 \leq pH \leq 4.5$ and $5 < pH \leq 7$. In the first region, the total cerium concentration in solution decreased from $1 \cdot 10^{-2}$ M at pH = 1.5, to $3 \cdot 10^{-4}$ M at pH = 4.5. Within the pH from 4.5 to 7, solubility behaviour remained pH-dependent, while, in this region, the dependence of ceria solubility on pH was more pronounced: from $3 \cdot 10^{-4}$ M to $6 \cdot 10^{-9}$ M. The log[Ce]-pH dependence could be linearized in these regions, with slopes of -0.5 and -2, respectively. To explain these phenomena, redox potential values were measured (Fig. 3b). According to these measurements, pe-pH dependence also consisted of two linear regions. The corresponding slopes could be fitted using linear equations $pe + 3.5pH = 27.5$ (at $2 \leq pH \leq 4.5$) and $pe + pH = 16$ (at $4.5 < pH \leq 7$). Hence, different ceria solubility behaviour at pH 1.5-4.5 and pH 4.5-7 could be associated with differing redox conditions.

In the upper range, $7 < pH \leq 12$, the concentration of cerium in the solution remained almost unchanged (Fig. 3a). The lowest measured cerium concentration in this pH range was 10^{-8} M.

Figure 4 shows HRTEM images of the solid phase after 1 month's equilibration of the initial ceria nanoparticles with aqueous phases at pH 3.1, pH 4.9 and pH 7.6. At pH 3.1 and pH 4.9, the morphology of initial truncated octahedral nanoparticles remained unchanged upon exposure with water, without any evidence of rounding or surface precipitation (Figure S_4 b,c). At pH 7.6 (Fig.4 c, d), transformation of initial nanoparticles to nanorods of varying length (50-200 nm) and 3 nm lateral size was observed, and only a small number of primary nanoparticles remained unchanged. According to electron diffraction (ED) data, interaction of ceria nanoparticles with aqueous phases did not result in any changes in phase composition of the all samples (Table S_1).

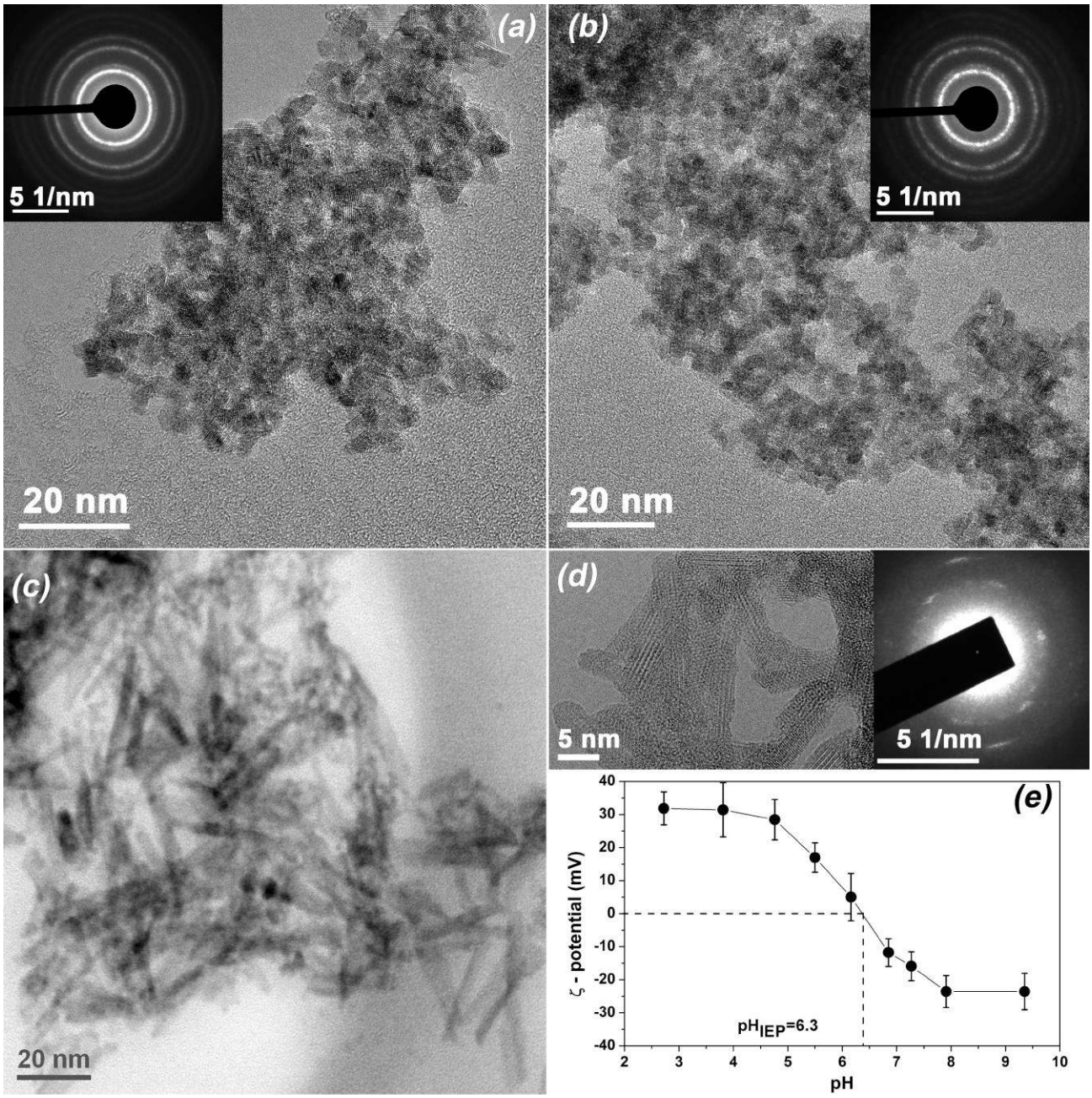

Figure 4. TEM images of ceria nanoparticles after 1 month's equilibration at (a) pH 3.1 (insert: SAED), (b) pH 4.9 (insert: SAED), and c,d) pH 7.6 (insert: typical nanobeam ED). e) pH-dependence of the ζ-potential for CeO_2 NPs in a 0.01M $NaClO_4$ solution.

CeO_2 nanoparticles usually possess octahedral habitus, because of the highly symmetric cubic structure of cerium dioxide (Fm3m). Nevertheless, numerous examples exist which demonstrate the formation of 1D ceria nanostructures (e.g. nanorods) under specific conditions [80-82]. The effect of

synthesis pH on ceria nanoparticle morphology is widely discussed in the literature [82, 83]. There are two main hypotheses explaining this phenomenon, namely classical Ostwald ripening [80] and a mixed mechanism involving sequential oriented attachment and the Ostwald ripening process [84]. Cerium dioxide particles synthesized without addition of any surfactants have a cubic or octahedral habitus. It is to be noted that, from the standpoint of classical Ostwald ripening theory, it is hard to explain the formation of highly anisotropic single crystalline micro- or nanoparticles having untypical habitus, such as quasi-one-dimensional nanorods of cerium dioxide. In turn, oriented attachment often leads to formation of 1D structures. This has been experimentally shown for different materials, including ceria [85, 86], and supported by theoretical calculations [87, 88]. Typically, formation of 1D nanoparticles proceeds in two stages. The first includes self-assembly of initial isotropic nanoparticles with formation of anisotropic aggregates. At the second stage, pseudo-single crystals are formed by the dissolution-recrystallization mechanism.

The formation of CeO_2 nanorods was observed in our experiments under neutral pH conditions. Taking into account the dependence of ceria nanoparticles' ζ-potential on pH and CeO_2 particle size distributions in 0.01 M $NaClO_4$ (Figure 4D, S_5), the colloidal stability of ceria nanoparticles in the acidic pH region is quite high, and their agglomeration is unlikely to proceed. Conversely, at pH values close to pH_{IEP} = 6.3, ceria nanoparticles become neutrally charged and form agglomerates of ~1 μm size, which can lead to their oriented attachment with subsequent Ostwald ripening. An HRTEM image of the nanorod where the second stage of formation (recrystallization) had not finished confirms this hypothesis (Figure S_4d).

Thermodynamic modeling of solubility data

In general, the equilibrium of solid metal dioxide with the aqueous solution is described by the following reaction:

$$MeO_2(s) + 2H_2O \leftrightarrows Me^{4+} + 4OH^- \quad (1)$$

with $\log K_{sp} = [Me^{4+}] \cdot [OH^-]^4$

This constant is the solubility product (K_{sp}) for a given medium, as the solubility and hydrolysis constant values strongly depend on the ionic strength of the solution; (in the present study, all the experiments were carried out at I=0.01M).

The total metal concentration that determines the solubility of the substance of interest includes the concentration of the Me^{4+} cation, and the concentration of all its hydrolysis products is given by:

$[Me(IV)]_{total} = [Me^{4+}] + \Sigma[Me(OH)_n^{4-n}]$

The hydrolysis reactions of Me^{4+} ions, i.e. the formation of $Me(OH)_n^{4-n}$ hydroxocomplexes, are usually written as:

$$Me^{4+} + nH_2O \leftrightarrows Me(OH)_n^{4-n} + nH^+ \quad (2)$$

The hydrolysis constants K_x (in a given medium) are defined by the following equation:

$K_x = [Me(OH)_n^{4-n}] \cdot [H^+]^n / [Me^{4+}]$,

where x indicates the stepwise hydrolysis reaction.

The above model is suitable for description of the pH-dependent dissolution of the substances consisting of elements whose oxidation state does not change upon dissolution [89-91]. According to the available Pourbaix diagram for cerium, at pH<7, the predominant cerium species in solutions is Ce(III) [92]. To verify this experimentally, XANES at the Ce-L_3-edge was used to analyze cerium oxidation states in the supernatant solution. Because of the limitations of this technique, only Ce concentrations higher that 10^{-4} M could be studied. Figure 5 shows experimental spectra for Ce-containing supernatant solutions at different pH values, together with reference spectra of Ce(III) and Ce(IV) compounds. The energy values and overall shape of the spectra provide strong evidence that Ce(III) is the only species existing in the solution under the chosen experimental conditions.

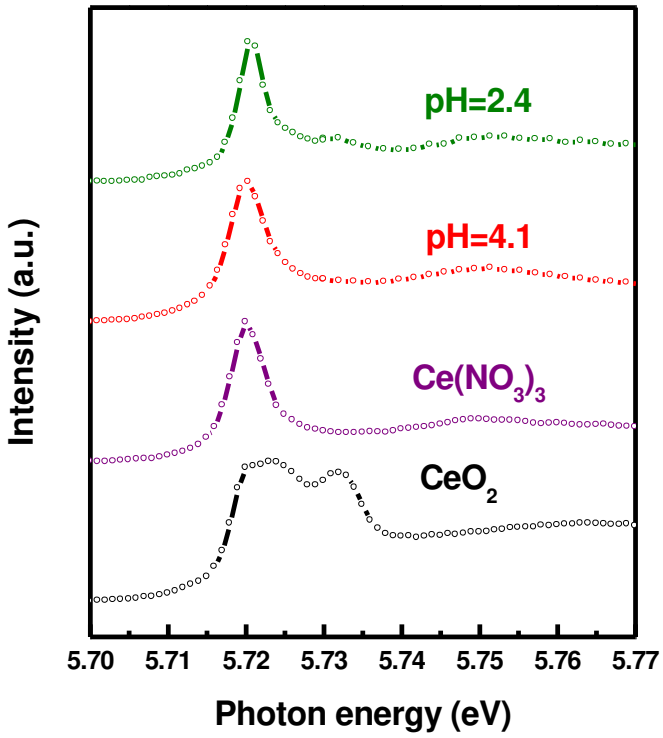

Figure 5. Ce-L_3-edge XANES spectra collected from supernatant solutions and standard samples (cerium(III) nitrate and cerium dioxide nanoparticles).

Based on these results, the reductive dissolution model was proposed for describing experimental data from $2 \leq pH \leq 7$. This model has been widely discussed in the literature, and observed for different compounds[93-98]. When the reduced form of a substance is thermodynamically stable, the redox reaction proceeds through interaction with the aqueous medium. In this case, water acts as a reducing agent. Such a process is typical for iron[93], lead[95] and plutonium[97] compounds.

Since Ce(III) is thermodynamically stable in the acidic pH region, and there is no additional reducing agent in the system, the solubility process can be described by the following equation:

$$CeO_2 + e^- + 4H^+ \leftrightarrows Ce^{3+} + 2H_2O \quad (3)$$

with $\log K_{CeO2/Ce3+} = \log[Ce^{3+}] + pe + 4pH$

The total cerium concentration in the solution is the sum of the concentrations of Ce^{3+} and its hydrolysis products:

$$[Ce(III)]_{total} = [Ce^{3+}] + [CeOH^{2+}] + [Ce(OH)_2^+] + [Ce(OH)_3]$$

Upon fitting the experimental data obtained in the acidic pH-region (where solubility behaviour is a function of pH), with known hydrolysis constants (Table 1) for Ce(III) [99] and experimental pe + pH values, the equilibrium constant for reductive dissolution reaction was established: $\log K_{CeO2/Ce3+}$ = -25.8 ± 0.3. It should be noted that this value describes both linear segments at $2 \leq pH \leq 7$: the segment with -0.5 slope (pe + 3.5pH = 27.5), and the segment with -2.0 slope (pe + pH = 16) (Figure 6, green line).

Combining equations (3)-(5) with the equilibrium constants for the ionic product of water ($\log K_w$ = 13.9) and for the Ce(IV)/Ce(III) redox couple ($\log K_{Ce(IV)/Ce(III)}$ = 21.9):

$$H_2O \leftrightarrows H^+ + OH^- \quad (4)$$

$$Ce^{4+} + e^- \leftrightarrows Ce^{3+} \quad (5)$$

yields:

$$CeO_2 + 2H_2O \leftrightarrows Ce^{4+} + 4OH^- \quad (6)$$

Hence, the experimental solubility product constant was calculated using the linear equation:

$$\log K_{sp} = \log K_{CeO2/Ce3+} + 4 \cdot \log K_w - \log K_{Ce(IV)/Ce(III)}, \quad (7)$$

and was found to be -59.3 ± 0.3. The value of the constant agrees well with theoretically estimated CeO_2 solubility product constant $\log K_{sp}$ = -60 [45].

The experimental solubility behaviour of CeO_2 in neutral and alkaline media ($7 < pH \leq 12$) is mostly pH independent. This can indicate that $Ce(OH)_4(aq)$ is a predominant cerium form in solution, under given conditions. The equilibrium between the solid and liquid phase can be described by the following reaction:

$$CeO_2 + 2H_2O \leftrightarrows Ce(OH)_4(aq) \quad (8)$$

The curve representing the results of modeling using the determined value of $\log K_{sp}$ and the values of the hydrolysis constants (see Table 1) is shown in Figure 6 (red line), along with the corresponding experimental data.

Table 1. Standard Ce(III) and Ce(IV) hydrolysis constants used to calculate ceria solubility

Reaction	logK_x	Reference
$Ce^{3+} + H_2O \leftrightarrows CeOH^{2+} + H^+$	-8,41±0,08	[99]
$Ce^{3+} + 2H_2O \leftrightarrows Ce(OH)_2^{+} + 2H^+$	-17,60±0,24	[99]
$Ce^{3+} + 3H_2O \leftrightarrows Ce(OH)_3(aq) + 3H^+$	-27,23±1,19	[99]
$Ce^{4+} + H_2O \leftrightarrows CeOH^{3+} + H^+$	0,764	[100]
$Ce^{4+} + 2H_2O \leftrightarrows Ce(OH)_2^{2+} + 2H^+$	0,048	[100]
$Ce^{4+} + 3H_2O \leftrightarrows Ce(OH)_3^{+} + 3H^+$	-1,485	[100]
$Ce^{4+} + 4H_2O \leftrightarrows Ce(OH)4(aq) + 4H^+$	-4,124	[100]

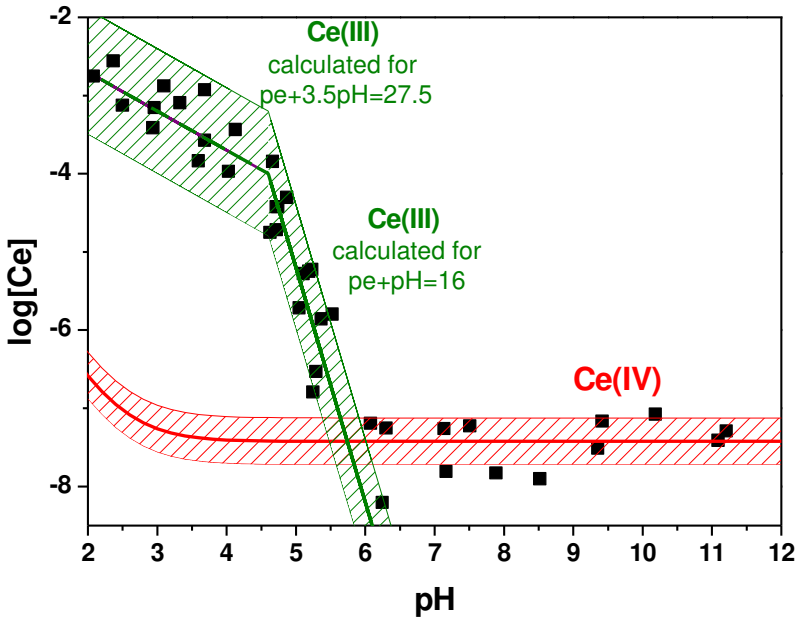

Figure 6. Experimental data for CeO_2 solubility in 0.01M $NaClO_4$, along with theoretical modeling. The green line corresponds to reductive dissolution (calculated using log$K_{CeO2/Ce3+}$= -25.8 ± 0.3); the red line corresponds to non-redox dissolution (calculated using logKsp = -59.3 ± 0.3).

Resulting from the difference in the Gibbs energy values for hydrated surface ions and the ions in the bulk of the particle, the molar Gibbs energy of formation depends strongly on particle size. This phenomenon is especially significant for particles of less than 10 nm in size. According to the Schindler equation[48], the difference between the standard molar Gibbs energies of small

nanocrystalline particles ($\Delta_f G°_m$(NP)) and bulk crystals of the same compound ($\Delta_f G°_m$(bulk)) could be written as follows:

$$\Delta_f G°_m(NP) = \Delta_f G°_m(bulk) + 2/3\gamma S, \quad (9)$$

where *S* is the surface area per mole of solid and γ stands for the free surface energy per surface area of the solid-liquid interface (interfacial tension). The γ component is directly proportional to the lnKsp value for the bulk compound; (for more details, see ref. [48]). The *S* component directly relates to particle diameter (*d)* and geometric factor (α), which depends on the shape of the particles:

$$S = M*\alpha/(\rho*d). \quad (10)$$

Here, *M* is the molecular weight and ρ the density of the solid.

Thus, any changes in the form factor of the ceria nanoparticles should, notably, affect their solubility. It can be supposed that formation of ceria nanorods in neutral and alkaline media causes an additional decrease in the solubility of ceria.

Ceria nanoparticles readily participate in redox processes involving reactive oxygen species (ROS)[26-33]. According to existing data, anti- and pro-oxidant activity of CeO_2 depends on non-stoichiometry of this material, (particularly non-stoichiometry caused by decreasing the particle size) [26-29], and on pH [30-33]. Such behaviour of CeO_2 currently remains poorly explained, while it is of great importance for biomedical applications of ceria, e.g. in cancer treatment. For example, Perez et al. [32] showed that CeO_2 nanoparticles are able to scavenge reactive oxygen species under neutral and alkaline pHs (pH > 7), but they are practically inactive against these species in acidic solutions. Similar results were reported later by Wason at al.[31]. It is well known that the cellular cancer environment is acidic in comparison with the neutral environment of normal cells [101-103]. pH values for normal tissues typically lie in the range of 7.2 – 7.6, while for tumours they are in the range of 5.6 – 7.6[104]. It is expected that CeO_2 nanoparticles could selectively protect normal cells from

oxidative stress, while promoting the formation of reactive oxygen species (e.g. hydrogen peroxide) in malignant cells.

The data obtained in the present work indicate that pH-dependent ceria activity is closely related to ceria dissolution. At pH < 7, the pro-oxidant activity of cerium dioxide can be attributed to reductive ceria dissolution, as described above. In the course of acidic dissolution, CeO_2 can even oxidize water. Conversely, according to the thermodynamic model developed and described in this paper, at pH > 7, $Ce(OH)_{4(aq)}$ is the only cerium species in solution. No redox reactions occur under these conditions and solubility of ceria is very low (within the range 10^{-7} - 10^{-8} M). ROS scavenging may occur only by their interaction with non-stoichiometric cerium oxide.

CONCLUSIONS

In this paper, we have established the experimental solubility curve for nanocrystalline cerium dioxide, using radiotracer and ICP-MS techniques. Using thermodynamic modeling, the solubility product constant was determined to be $\log K_{sp} = -59.3 \pm 0.3$ under the selected conditions. This K_{sp} value fits experimental data successfully in all pH regions, taking into account the concept of CeO_2 reductive dissolution.

SUPPOROTING INFORMATION

Kinetics of CeO_2 dissolution at different pHs and ceria concentrations; comparison of ceria solubility data at different times of equilibration; experimental SAXS data and fitting for ceria suspension; XPS spectra of nanosized CeO_2; TEM images of ceria nanoparticles after equilibration for 1 month at different pHs; CeO_2 particles size distributions in 0.01M $NaClO_4$ at different pHs measured by DLS technique; the interplanar distances for CeO_2 calculated from ED. This material is available free of charge via the Internet at http://pubs.acs.org/.

ACKNOWLEDGEMENTS. The study was funded by RFBR, according to the research projects No. 16-31-06000 mol_a_dk and No. 16-33-00650 mol_a. The authors would like to thank the M.V.

Lomonosov Moscow State University Programme of Development and A. V. Garshev for partial support of HRTEM measurements. We are also grateful to the "Nanochemistry and Nanomaterials" user facility of the Department of Chemistry of MSU for providing the HRTEM and XPS measurements. SAXS measurements were performed using equipment of CKP FMI IPCE RAS. SGM and DKS were supported by the Director, Office of Science, Office of Basic Energy Sciences (BES), Division of Chemical Sciences, Geosciences, and Biosciences (CSGB) Heavy Element Chemistry Programme of the U.S. Department of Energy (DOE) at the Lawrence Berkeley National Laboratory (LBNL), under Contract No. DE-AC02-05CH11231. MES Beamline 11.0.2.2 at the ALS was supported by the Director, Office of Science, BES, CSGB Condensed Phase and Interfacial Molecular Sciences Programme by the U.S. DOE at LBNL, under Contract No. DE-AC02-05CH11231. The ALS and TT were supported by the Director, Office of Science, BES, of the U.S. DOE, under Contract No. DE-AC02-05CH11231 at LBNL.

REFERENCES

1. Liu, C.-N.; Wiesener, M.; Giner, I.; Grundmeier, G. Structure and Corrosion Resistance of Cerium-Oxide Films on AZ31 as Deposited by High-Power Ultrasound Supported Conversion Chemistry. *Front. Mater.* **2015,** *2*, 68-78.
2. Ivanov, V. K.; Polezhaeva, O. S.; Tret'yakov, Y. D. Nanocrystalline ceria: Synthesis, Structure-Sensitive Properties, and Promising Applications. *Russ. J. Gen. Chem.* **2010,** *80*, 604-617.
3. Montini, T.; Melchionna, M.; Monai, M.; Fornasiero, P. Fundamentals and Catalytic Applications of CeO_2-Based Materials. *Chem. Rev.* **2016,** *116*, 5987–6041.
4. Anupriya, K.; Vivek, E.; Subramanian, B. Facile Synthesis of Ceria Nanoparticles by Precipitation Route for UV Blockers. *J. Alloys Compd.* **2014,** *590*, 406-410.
5. Zholobak, N. M.; Ivanov, V. K.; Shcherbakov, A. B.; Shaporev, A. S.; Polezhaeva, O. S.; Baranchikov, A. Y.; Spivak, N. Y.; Tretyakov, Y. D. UV-Shielding Property, Photocatalytic Activity and Photocytotoxicity of Ceria Colloid Solutions. *J. Photochem. Photobiol. B* **2011,** *102*, 32-38.
6. Kharton, V. V.; Figueiredo, F. M.; Navarro, L.; Naumovich, E. N.; Kovalevsky, A. V.; Yaremchenko, A. A.; Viskup, A. P.; Carneiro, A.; Marques, F. M. B.; Frade, J. R. Ceria-Based Materials for Solid Oxide Fuel Cells. *J. Mater. Sci.* **2001,** *36*, 1105-1117.
7. Badwal, S. P. S.; Fini, D.; Ciacchi, F. T.; Munnings, C.; Kimpton, J. A.; Drennan, J. Structural and Microstructural Stability of Ceria - Gadolinia Electrolyte Exposed to Reducing Environments of High Temperature Fuel Cells. *J. Mater. Chem. A* **2013,** *1*, 10768-10782.
8. Celardo, I.; Pedersen, J. Z.; Traversa, E.; Ghibelli, L. Pharmacological Potential of Cerium Oxide Nanoparticles. *Nanoscale* **2011,** *3*, 1411-1420.

9. Zholobak, N. M.; Shcherbakov, A. B.; Vitukova, E. O.; Yegorova, A. V.; Scripinets, Y. V.; Leonenko, I. I.; Baranchikov, A. Y.; Antonovich, V. P.; Ivanov, V. K. Direct Monitoring of the ROS-Nanoceria Interaction in Living Cells. *RSC Advances* **2014,** *4*, 51703-51710.
10. Walkey, C.; Das, S.; Seal, S.; Erlichman, J.; Heckman, K.; Ghibelli, L.; Traversa, E.; McGinnis, J. F.; Self, W. T. Catalytic Properties and Biomedical Applications of Cerium Oxide Nanoparticles. *Environ. Sci. Nano* **2015,** *2*, 33-53.
11. Ivanov, V. K.; Shcherbakov, A. B.; Usatenko, A. V. Structure-Sensitive Properties and Biomedical Applications of Nanodispersed Cerium Dioxide. *Russ. Chem. Rev.* **2009,** *78* (9), 855-871.
12. Jiang, L.; Yao, M.; Liu, B.; Li, Q.; Liu, R.; Lv, H.; Lu, S.; Gong, C.; Zou, B.; Cui, T. et al Controlled Synthesis of CeO_2/Graphene Nanocomposites with Highly Enhanced Optical and Catalytic Properties. *J. Phys. Chem. C* **2012,** *116*, 11741-11745.
13. Xijuan, Y.; Pingbo, X.; Qingde, S. Size-Dependent Optical Properties of Nanocrystalline CeO_2:Er Obtained by Combustion Synthesis. *Phys. Chem. Chem. Phys.* **2001,** *3*, 5266-5269.
14. Sharma, A.; Varshney, M.; Park, J.; Ha, T. K.; Chae, K. H.; Shin, H. J. Bifunctional $Ce_{1-x}Eu_xO_2$ ($0 \leq x \leq 0.3$) Nanoparticles for Photoluminescence and Photocatalyst Applications: An X-ray Absorption Spectroscopy Study. *Phys. Chem. Chem. Phys.* **2015,** *17*, 30065-30075.
15. Shishkin, M.; Ziegler, T. Direct Modeling of the Electrochemistry in the Three-phase Boundary of Solid Oxide Fuel Cell Anodes by Density Functional Theory: A Critical Overview. *Phys. Chem. Chem. Phys.* **2014,** *16*, 1798-1808.
16. Machida, M.; Kawada, T.; Fujii, H.; Hinokuma, S. The Role of CeO_2 as a Gateway for Oxygen Storage over CeO_2-Grafted Fe_2O_3 Composite Materials. *J. Phys. Chem. C* **2015,** *119*, 24932-24941.
17. Imagawa, H.; Suda, A.; Yamamura, K.; Sun, S. Monodisperse CeO_2 Nanoparticles and Their Oxygen Storage and Release Properties. *J. Phys. Chem. C* **2011,** *115*, 1740-1745.
18. Han, X.; Amrane, N.; Zhang, Z.; Benkraouda, M. Oxygen Vacancy Ordering and Electron Localization in CeO_2: Hybrid Functional Study. *J. Phys. Chem. C* **2016,** *120*, 13325-13331.
19. Barrios, A. C.; Rico, C. M.; Trujillo-Reyes, J.; Medina-Velo, I. A.; Peralta-Videa, J. R.; Gardea-Torresdey, J. L. Effects of Uncoated and Citric Acid Coated Cerium Oxide Nanoparticles, Bulk Cerium Oxide, Cerium Acetate, and Citric Acid on Tomato Plants. *Sci. Total Environ.* **2016,** *563–564,* 956–964.
20. Li, Y.; Li, P.; Yu, H.; Bian, Y. Recent Advances (2010–2015) in Studies of Cerium Oxide Nanoparticles' Health Effects. *Environ. Toxicol. Pharmacol.* **2016,** *44*, 25-29.
21. Zhang, W.; Musante, C.; White, J. C.; Schwab, P.; Wang, Q.; Ebbs, S. D.; Ma, X. Bioavailability of Cerium Oxide Nanoparticles to Raphanus Sativus L. in Two Soils. *Plant Physiol. Biochem.* **2015**, DOI: 10.1016/j.plaphy.2015.12.013.
22. García, A.; Espinosa, R.; Delgado, L.; Casals, E.; González, E.; Puntes, V.; Barata, C.; Font, X.; Sánchez, A. Acute Toxicity of Cerium Oxide, Titanium Oxide and Iron Oxide Nanoparticles Using Standardized Tests. *Desalination* **2011,** *269*, 136-141.
23. Auffan, M.; Rose, J.; Orsiere, T.; De Meo, M.; Thill, A.; Zeyons, O.; Proux, O.; Masion, A.; Chaurand, P.; Spalla, O. et al. CeO_2 Nanoparticles Induce DNA Damage Towards Human Dermal Fibroblasts in vitro. *Nanotoxicology* **2009,** *3*, 161–169.
24. Jakupec, M. A.; Unfried, P.; Keppler, B. K. Pharmacological Properties of Cerium Compunds. *Rev. Physiol., Biochem. Pharmacol.* **2005,** *153*, 101-111.
25. Shannon, R. Revised Effective Ionic Radii and Systematic Studies of Interatomic Distances in Halides and Chalcogenides. *Acta Cryst.* **1976,** *A32*, 751–767.
26. Shcherbakov, A. B.; Zholobak, N. M.; Ivanov, V. K.; Ivanova, O. S.; Marchevsky, A. V.; Baranchikov, A. E.; Spivak, N. Y.; Tretyakov, Y. D. Synthesis and Antioxidant Activity of

Biocompatible Maltodextrin-Stabilized Aqueous Sols of Nanocrystalline Ceria. *Russ. J. Inorg. Chem.* **2012,** *57*, 1411-1418.
27. Pirmohamed, T.; Dowding, J. M.; Singh, S.; Wasserman, B.; Heckert, E.; Karakoti, A. S.; King, J. E. S.; Seal, S.; Self, W. T. Nanoceria Exhibit Redox State-Dependent Catalase Mimetic Activity. *Chem. Commun.* **2010,** *46*, 2736-2738.
28. Tsai, Y.; Oca-Cossio, J.; Agering, K.; Simpson, N. E.; Atkinson, M. A.; Wasserfall, C. H.; Constantinidis, I.; Sigmund, W. Novel Synthesis of Cerium Oxide Nanoparticles for Free Radical Scavenging. *Nanomedicine* **2007** *2*, 325 - 332.
29. Korsvik, C.; Patil, S.; Seal, S.; Self, W. T. Superoxide Dismutase Mimetic Properties Exhibited by Vacancy Engineered Ceria Nanoparticles. *Chem. Commun.* **2007,** *10*, 1056-1058.
30. Asati, A.; Santra, S.; Kaittanis, C.; Nath, S.; Perez, J. M. Oxidase Activity of Polymer-Coated Cerium Oxide Nanoparticles. *Angew. Chem. Int. Ed.* **2009,** *48*, 2308–2312.
31. Wason, M. S.; Colon, J.; Das, S.; Seal, S.; Turkson, J.; Zhao, J.; Baker, C. H. Sensitization of Pancreatic Cancer Cells to Radiation by Cerium Oxide Nanoparticle-Induced ROS Production. *Nanomedicine: NBM* **2013,** *9*, 558-569.
32. Perez, J. M.; Asati, A.; Nath, S.; Kaittanis, C. Synthesis of Biocompatible Dextran-Coated Nanoceria with pH-Dependent Antioxidant Properties. *Small* **2008,** *4*, 552-556.
33. Jiao, X.; Song, H.; Zhao, H.; Bai, W.; Zhang, L.; Lv, Y. Well-redispersed Ceria Nanoparticles: Promising Peroxidase Mimetics for H_2O_2 and Glucose Detection. *Anal. Methods* **2012,** *4*, 3261-3267.
34. Deshpande, S.; Patil, S.; Kuchibhatla, S. V.; Seal, S. Size Dependency Variation in Lattice Parameter and Valency States in Nanocrystalline Cerium Oxide. *Appl. Phys. Lett.* **2005,** *87*, 87-89.
35. Zhang, F.; Wang, P.; Koberstein, J.; Khalid, S.; Chan, S.-W. Cerium Oxidation State in Ceria Nanoparticles Studied with X-ray Photoelectron Spectroscopy and Absorption Near Edge Spectroscopy. *Surf. Sci.* **2004,** *563*, 74-82.
36. Paparazzo, E. On the Curve-Fitting of XPS Ce(3d) Spectra of Cerium Oxides. *Mater. Res. Bull.* **2011,** *46*, 323-326.
37. Paun, C.; Safonova, O. V.; Szlachetko, J.; Abdala, P. M.; Nachtegaal, M.; Sa, J.; Kleymenov, E.; Cervellino, A.; Krumeich, F.; van Bokhoven, J. A. Polyhedral CeO_2 Nanoparticles: Size-Dependent Geometrical and Electronic Structure. *J. Phys. Chem. C* **2012,** *116*, 7312-7317.
38. Cafun, J.-D.; Kvashnina, K. O.; Casals, E.; Puntes, V. F.; Glatzel, P. Absence of Ce^{3+} Sites in Chemically Active Colloidal Ceria Nanoparticles. *ACS Nano* **2013,** *7*, 10726-10732.
39. Goris, B.; Turner, S.; Bals, S.; Van Tendeloo, G. Three-Dimensional Valency Mapping in Ceria Nanocrystals. *ACS Nano* **2014,** *8*, 10878-10884.
40. Dahle, J. T.; Livi, K.; Arai, Y. Effects of pH and Phosphate on CeO_2 Nanoparticle Dissolution. *Chemosphere* **2015,** *119*, 1365-1371.
41. Stoianov, O. O.; Ivanov, V. K.; Shcherbakov, A. B.; Stoyanova, I. V.; Chivireva, N. A.; Antonovich, V. P. Determination of Cerium(III) and Cerium(IV) in Nanodisperse Ceria by Chemical Methods. *Russ. J. Inorg. Chem.* **2014,** *59* (2), 15-23.
42. Tsunekawa, S.; Sivamohan, R.; Ito, S.; Kasuya, A.; Fukuda, T. Structural Study on Monosize CeO_{2-x} Nano-Particles. *Nanostruct. Mater.* **1999,** *11*, 141-147.
43. Tsunekawa, S.; Sahara, R.; Kawazoe, Y.; Ishikawa, K. Lattice Relaxation of Monosize CeO_{2-x} Nanocrystalline Particles. *Appl. Surf. Sci.* **1999,** *152*, 53-56.
44. Tsunekawa, S.; Sivamohan, R.; Ohsuga, T.; Kasuya, A.; Takahashi, H.; Tohji, K. Ultraviolet Absorption Spectra of CeO_2 Nano-Particles *Mater. Sci. Forum.* **1999,** *315–317*, 439–445.
45. Curti, E.; Degueldre, C. Solubility and Hydrolysis of Zr Oxides: A Review and Supplemental Data. *Radiochim. Acta* **2002,** *90*, 801-804.

46. Cornelis, G.; Ryan, B.; McLaughlin, M. J.; Kirby, J. K.; Beak, D.; Chittleborough, D. Solubility and Batch Retention of CeO_2 Nanoparticles in Soils. *Environ. Sci. Technol.* **2011,** *45*, 2777-2782.
47. Graham, U. M.; Tseng, M. T.; Jasinski, J. B.; Yokel, R. A.; Unrine, J. M.; Davis, B. H.; Dozier, A. K.; Hardas, S. S.; Sultana, R.; Grulke, E. A. et al. In Vivo Processing of Ceria Nanoparticles inside Liver: Impact on Free-Radical Scavenging Activity and Oxidative Stress. *ChemPlusChem.* **2014,** *79*, 1083-1088.
48. Schindler, P. W., *Heterogeneous Equilibria Involving Oxides, Hydroxides, Carbonates, and Hydroxide Carbonates*; American Chemical Society: Washington, D. C., 1967.
49. Baranchikov, A. E.; Polezhaeva, O. S.; Ivanov, V. K.; Tretyakov, Y. D. Lattice Expansion and Oxygen Non-Stoichiometry of Nanocrystalline Ceria. *CrystEngComm* **2010,** *12*, 3531-3533.
50. Aliev, R. A.; Ermolaev, S. V.; Vasiliev, A. N.; Ostapenko, V. S.; Lapshina, E. V.; Zhuikov, B. L.; Zakharov, N. V.; Pozdeev, V. V.; Kokhanyuk, V. M.; Myasoedov, B. F. et al. Isolation of Medicine-Applicable Actinium-225 from Thorium Targets Irradiated by Medium-Energy Protons. *Solvent Extr. Ion Exch.* **2014,** *32*, 468-477.
51. Lake, J. A. An Iterative Method of Slit-Correcting Small Angle X-ray Data. *Acta Cryst.* **1967,** *23*, 191-194.
52. Bluhm, H.; Andersson, K.; Araki, T.; Benzerara, K.; Brown, G. E.; Dynes, J. J.; Ghosal, S.; Gilles, M. K.; Hansen, H. C.; Hemminger, J. C. et al. Soft X-ray Microscopy and Spectroscopy at the Molecular Environmental Science Beamline at the Advanced Light Source. *J. Electron. Spectrosc. Relat. Phenom.* **2006,** *150*, 86-104.
53. Kilcoyne, A. L. D.; Tyliszczak, T.; Steele, W. F.; Fakra, S.; Hitchcock, P.; Franck, K.; Anderson, E.; Harteneck, B.; Rightor, E. G.; Mitchell, G. E. et al. Interferometer-Controlled Scanning Transmission X-ray Microscopes at the Advanced Light Source. *J. Synchrotron Rad.* **2003,** *10*, 125-136.
54. Tyliszczak, T.; Warwick, T.; Kilcoyne, A. L. D.; Fakra, S.; Shuh, D. K.; Yoon, T. H.; Brown Jr., G. E.; Andrews, S.; Chembrolu, V.; Strachan, J. et al. Soft X-ray Scanning Transmission Microscope Working in an Extended Energy Range at the Advanced Light Source. *AIP Conf. Proc.* **2004,** *705*, 1356-1359.
55. Bugaris, D. E.; Copping, R.; Tyliszczak, T.; Shuh, D. K.; Ibers, J. A. $La_2U_2Se_9$: An Ordered Lanthanide/Actinide Chalcogenide with a Novel Structure Type. *Inorg. Chem.* **2010,** *49*, 2568-2575.
56. Meihaus, K. R.; Minasian, S. G.; Lukens, W. W.; Kozimor, S. A.; Shuh, D. K.; Tyliszczak, T.; Long, J. R. Influence of Pyrazolate vs N-Heterocyclic Carbene Ligands on the Slow Magnetic Relaxation of Homoleptic Trischelate Lanthanide(III) and Uranium(III) Complexes. *J. Am. Chem. Soc.* **2014,** *136*, 6056-6068.
57. Zhang, F.; Chan, S.-W.; Spanier, J. E.; Apak, E.; Jin, Q. Cerium Oxide Nanoparticles: Size-Selective Formation and Structure Analysis. *Appl. Phys. Lett.* **2002,** *80*, 126-129.
58. Tsunekawa, S.; Ishikawa, K.; Li, Z.-Q.; Kawazoe, Y.; Kasuya, A. Origin of Anomalous Lattice Expansion in Oxide Nanoparticles. *Phys. Rev. Lett.* **2000,** *85*, 3440-3443.
59. Hailstone, R. K.; DiFrancesco, A. G.; Leong, J. G.; Allston, T. D.; Reed, K. J. A Study of Lattice Expansion in CeO_2 Nanoparticles by Transmission Electron Microscopy. *J. Phys. Chem. C* **2009,** *113*, 15155-15159.
60. Fronzi, M.; Soon, A.; Delley, B.; Traversa, E.; Stampfl, C. Stability and Morphology of Cerium Oxide Surfaces in an Oxidizing Environment: A first-principles investigation. *J. Chem. Phys.* **2009,** *131*, 104701.
61. Sayle, T. X. T.; Parker, S. C.; Sayle, D. C. Shape of CeO_2 Nanoparticles Using Simulated Amorphisation and Recrystallisation. *Chem. Commun.* **2004,** 2438-2439.

62. Tan, J. P. Y.; Tan, H. R.; Boothroyd, C.; Foo, Y. L.; He, C. B.; Lin, M. Three-Dimensional Structure of CeO_2 Nanocrystals. *J. Phys. Chem. C* **2011,** *115*, 3544-3551.
63. Willard, M. A.; Kurihara, L. K.; Carpenter, E. E.; Calvin, S.; Harris, V. G. Chemically Prepared Magnetic Nanoparticles. *Int. Mat. Rev.* **2004,** *49*, 145–147.
64. Svergun, D. I. Determination of the Regularization Parameter in Indirect-Transform Methods Using Perceptual Criteria. *J. Appl. Crystallogr.* **1992,** *25*, 495-503.
65. Altman, A. B.; Pacold, J. I.; Wang, J.; Lukens, W. W.; Minasian, S. G. Evidence for 5d-σ and 5d-π Covalency in Lanthanide Sesquioxides from Oxygen K-edge X-ray Absorption Spectroscopy. *Dalton Trans.* **2016,** *45,* 9948-9961.
66. Loble, M. W.; Keith, J. M.; Altman, A. B.; Stieber, S. C. E.; Batista, E. R.; Boland, K. S.; Conradson, S. D.; Clark, D. L.; Pacheco, J. L.; Kozimor, S. A. et al. Covalency in Lanthanides. An X-ray Absorption Spectroscopy and Density Functional Theory Study of $LnCl_6^{x-}$ (x=3, 2). *J. Am. Chem. Soc.* **2015,** *137*, 2506-2523.
67. Shuh, D. K.; Terminello, L. J.; Boatner, L. A.; Abraham, M. M.; Perry, D. Characterization of Ce-Doped $LaPO_4$ by X-ray Absorption Spectroscopy. *New Materials for Advanced Solid State Lasers. Symposium* **1994**, 91-96.
68. Garvie, L. A. J.; Buseck, P. R. Determination of Ce^{4+}/Ce^{3+} in Electron-Beam-Damaged CeO_2 by Electron Energy-Loss Spectroscopy. *J. Phys. Chem. Solids* **1999,** *60* , 1943-1947.
69. Wu, Z. Y.; Jollet, F.; Gota, S.; Thromat, N.; Gautier-Soyer, M.; Petit, T. X-ray Absorption at the Oxygen K Edge in Cubic f Oxides Examined Using a Full Multiple-Scattering Approach. *J. Phys.: Condens. Matter* **1999,** *11*, 7185.
70. Chen, J.; Chen, Z.; Wei, Y. Formation Mechanism of the Slice and Rod-like Cerium Dioxide Precursor Particles. *Mater. Sci. Forum* **2013,** *743-744*, 389-396.
71. Howald, L.; Stilp, E.; de Réotier, P. D.; Yaouanc, A.; Raymond, S.; Piamonteze, C.; Lapertot, G.; Baines, C.; Keller, H. Evidence for Coexistence of Bulk Superconductivity and Itinerant Antiferromagnetism in the Heavy Fermion System $CeCo(In_{1-x}Cd_x)_5$. *Sci. Rep.* **2015,** *5*, 12528.
72. Kaindl, G.; Kalkowski, G.; Brewer, W. D.; Perscheid, B.; Holtzberg, F. M-Edge X-ray Absorption Spectroscopy of 4f Instabilities in Rare-Earth Systems. *J. Appl. Phys.* **1984,** *55*, 1910-1915.
73. Kotani, A.; Ogasawara, H. Theory of Core-Level Spectroscopy of Rare-Earth Oxides. *J. Electron. Spectrosc. Relat. Phenom.* **1992,** *60*, 257-299.
74. Paparazzo, E. XPS studies of Damage Induced by X-ray Irradiation on CeO_2 Surfaces. *Surf. Sci. Lett.* **1990,** *234*, L253-L258.
75. Paparazzo, E.; Ingo, G. M.; Zacchetti, N. X-ray Induced Reduction Effects at CeO_2 Surfaces: An X-ray Photoelectron Spectroscopy Study. *J. Vac. Sci. Technol. A* **1991,** *9*, 1416-1420.
76. Kónya, J.; Nagy, N. M. Determination of Water-Soluble Phosphate Content of Soil Using Heterogeneous Exchange Reaction with ^{32}P Radioactive Tracer. *Soil. Till. Res.* **2015,** *150*, 171-179.
77. Gelsema, W. J.; Remijnse, A. G. A Study on the Effect of Labelling on the Solubility of Cerium(III) Oxalate in Water: On the Feasibility of the Radiometric Determination of Solubility. *Recl. Trav. Chim. Pays-Bas* **1971,** *90*, 213-220.
78. Morgan, A.; Holmes, A.; Gold, C. Studies of the Solubility of Constituents of Chrysotile Asbestos in vivo Using Radioactive Tracer Techniques. *Environ. Res.* **1971,** *4*, 558-570.
79. Altmaier, M.; Neck, V.; Fanghänel, T. Solubility of Zr(IV), Th(IV) and Pu(IV) Hydrous Oxides in $CaCl_2$ Solutions and the Formation of Ternary Ca-M(IV)-OH Complexes. *Radiochim. Acta* **2008,** *96*, 541-550.

80. Pan, C.; Zhang, D.; Shi, L.; Fang, J. Template-Free Synthesis, Controlled Conversion, and CO Oxidation Properties of CeO_2 Nanorods, Nanotubes, Nanowires, and Nanocubes. *Eur. J. Inorg. Chem.* **2008,** *2008*, 2429-2436.
81. Ono, Y.; Fujii, H. Low-temperature Synthesis of Cerium Oxide Nanorods and Their Suppressive Effect on Photocatalysis of Titanium Dioxide. *Ceram. Int.* **2015,** *41*, 15231-15234.
82. Torrente-Murciano, L.; Gilbank, A.; Puertolas, B.; Garcia, T.; Solsona, B.; Chadwick, D. Shape-Dependency Activity of Nanostructured CeO_2 in the Total Oxidation of Polycyclic Aromatic Hydrocarbons. *Appl. Catal. B* **2013,** *132–133*, 116-122.
83. Ji, Z.; Wang, X.; Zhang, H.; Lin, S.; Meng, H.; Sun, B.; George, S.; Xia, T.; Nel, A. E.; Zink, J. I. Designed Synthesis of CeO_2 Nanorods and Nanowires for Studying Toxicological Effects of High Aspect Ratio Nanomaterials. *ACS Nano* **2012,** *6*, 5366-5380.
84. Du, N.; Zhang, H.; Chen, B.; Ma, X.; Yang, D. Ligand-free Self-Assembly of Ceria Nanocrystals into Nanorods by Oriented Attachment at Low Temperature. *J. Phys. Chem. C* **2007,** *111*, 12677-12680.
85. De Yoreo, J. J.; Gilbert, P. U. P. A.; Sommerdijk, N. A. J. M.; Penn, R. L.; Whitelam, S.; Joester, D.; Zhang, H.; Rimer, J. D.; Navrotsky, A.; Banfield, J. F. et al. Crystallization by Particle Attachment in Synthetic, Biogenic, and Geologic Environments. *Science* **2015,** *349*, aaa6760.
86. Ivanov, V. K.; Fedorov, P. P.; Baranchikov, A. Y.; Osiko, V. V. Oriented Attachment of Particles: 100 Years of Investigations of Non-Classical Crystal Growth. *Russ. Chem. Rev.* **2014,** *83*, 1204-1222.
87. Sathiyanarayanan, R.; Alimohammadi, M.; Zhou, Y.; Fichthorn, K. A. Role of Solvent in the Shape-Controlled Synthesis of Anisotropic Colloidal Nanostructures. *J. Phys. Chem. C* **2011,** *115*, 18983-18990.
88. Fichthorn, K. A. Molecular Phenomena in Colloidal Nanostructure Synthesis. *Mol. Simul.* **2014,** *40* (1-3), 134-140.
89. Neck, V.; Altmaier, M.; Müller, R.; Bauer, A.; Fanghänel, T.; Kim, J. I. Solubility of Crystalline Thorium Dioxide. *Radiochim. Acta* **2003,** *91*, 253-262.
90. Kobayashi, T.; Sasaki, T.; Takagi, I.; Moriyama, H. Solubility of Zirconium(IV) Hydrous Oxides. *J. Nucl. Sci. Technol.* **2007,** *44*, 90-94.
91. Rai, D.; Yui, M.; Schaef, H. T.; Kitamura, A. Thermodynamic Model for SnO_2(cr) and SnO_2(am) Solubility in the Aqueous Na^+–H^+–OH^-–Cl^-–H_2O System. *J. Solution Chem.* **2011,** *40*, 1155-1172.
92. Hayes, S. A.; Yu, P.; O'Keefe, T. J.; O'Keefe, M. J.; Stoffer, J. O. The Phase Stability of Cerium Species in Aqueous Systems: I. E-pH Diagram for the Ce-$HClO_4$-H_2O System. *J. Electrochem. Soc.* **2002,** *149*, 623-630.
93. Schwertmann, U., *Solubility and Dissolution of Iron Oxides*; Springer: Netherlands, 1991.
94. Dos Santos Afonso, M.; Stumm, W. Reductive Dissolution of Iron(III) (Hydr)Oxides by Hydrogen Sulfide. *Langmuir* **1992,** *8*, 1671-1675.
95. Wang, Y.; Wu, J.; Wang, Z.; Terenyi, A.; Giammar, D. E. Kinetics of Lead(IV) Oxide (PbO_2) Reductive Dissolution: Role of Lead(II) Adsorption and Surface Speciation. *J. Colloid Interface Sci.* **2013,** *389*, 236-243.
96. Neck, V.; Altmaier, M.; Fanghänel, T. Solubility of Plutonium Hydroxides/Hydrous Oxides under Reducing Conditions and in the Presence of Oxygen. *C. R. Chim.* **2007,** *10*, 959-977.
97. Neck, V.; Altmaier, M.; Seibert, A.; Yun, J. I.; Marquardt, C. M. Solubility and Redox Reactions of Pu(IV) Hydrous Oxide: Evidence for the Formation of PuO_{2+x}(s, hyd). *Radiochim. Acta* **2007,** *95*, 193–207.
98. Revesz, E.; Fortin, D.; Paktunc, D. Reductive Dissolution of Arsenical Ferrihydrite by Bacteria. *Appl. Geochem.* **2016,** *66*, 129-139.

99. Lee, J. H.; Byrne, R. H. Examination of Comparative Rare Earth Element Complexation Behavior Using Linear Free-Energy Relationships. *Geochim. Cosmochim. Acta* **1992,** *56*, 1127-1137.
100. Bilal, B. A.; Muller, E. Thermodynamic Study of Cerium(4+)/Cerium(3+) Redox Reaction in Aqueous Solutions at Elevated Temperatures. *Z. Naturforsch. A: Phys. Sci.* **1992,** *47*, 974-984.
101. Gerweck, L. E.; Seetharaman, K. pH Gradient in Tumor versus Normal Tissue: Potential Exploitation for the Treatment of Cancer. *Cancer Res.* **1996,** *56*, 1194-8.
102. Engin, K.; Leeper, D. B.; Cater, J. R.; Thistlethwaite, A. J.; Tupchong, L.; McFarlane, J. D. Extracellular pH Distribution in Human Tumours. *Int. J. Hyperthermia* **1995,** *11*, 211-216.
103. Helmlinger, G.; Yuan, F.; Dellian, M.; Jain, R. K. Interstitial pH and pO_2 Gradients in Solid Tumors in vivo: High-Resolution Measurements Reveal a Lack of Correlation. *Nat. Med.* **1997** *3*, 177-182.
104. Griffiths, J. R. Are Cancer Cells Acidic? *Br. J. Cancer.* **1991,** *64*, 425-427.